

CNN Sensor Analytics with Hybrid-Float6 on Low-Power Resource-Constrained Embedded FPGAs.

Corresponding author: Yarib Nevarez (e-mail: nevarez@item.uni-bremen.de).

This work is funded by the Consejo Nacional de Ciencia y Tecnología - CONACYT

ABSTRACT The use of artificial intelligence (AI) in sensor analytics is entering a new era based on the use of ubiquitous embedded connected devices. This transformation requires the adoption of design techniques that reconcile accurate results with sustainable system architectures. As such, improving the efficiency of AI hardware engines as well as machine learning (ML) compatibility must be considered. In this paper, we present the Hybrid-Float6 (HF6) quantization and its dedicated hardware design. We propose an optimized multiply-accumulate (MAC) hardware by reducing the mantissa multiplication to a multiplexor-adder operation. We exploit the intrinsic error tolerance of ANN to further reduce the hardware design with approximation. To preserve model accuracy, we present a quantization-aware training (QAT) method, which in some cases improves accuracy. We demonstrate this concept in 2D convolution layers. We present a lightweight tensor processor (TP) implementing a pipelined vector dot-product. For ML compatibility/portability, the 6-bit FP is wrapped in the standard FP format, which is automatically extracted by the proposed hardware. The hardware/software architecture is compatible with TensorFlow (TF) Lite. We evaluate the applicability of our approach with a CNN-regression model for anomaly localization in a structural health monitoring (SHM) application. The embedded hardware/software framework is demonstrated on XC7Z007S as the smallest Zynq-7000 SoC. The proposed implementation achieves a peak power efficiency and acceleration of 5.7 GFLOPS/s/W and 48.3 \times , respectively.

INDEX TERMS Convolutional neural networks, structural health monitoring, hardware accelerator, TensorFlow Lite, embedded systems, FPGA, custom floating-point

I. INTRODUCTION

THERE is a growing demand for ubiquitous AI sensor analytics. Industry 4.0 and smart city infrastructure leverage AI solutions to increase productivity and adaptability [1]. These solutions are powered by advances in ML, compute engines, and big data. Hence, improvements of these should be considered for research, as they are the machinery of the future.

Convolutional neural networks (CNNs) represent the essential building blocks in 2D pattern analytics. Sensor-based applications such as mechanical fault diagnosis [2], [3], structural health monitoring [4], human activity recognition (HAR) [5], hazardous gas detection [6] have been powered by CNN models in industry and academia. CNN-based models, as one of the main types of artificial neural networks (ANNs), have been widely used in sensor analytics with automatic learning from sensor data [7]–[10]. In this context, CNN models are applied for automatic feature learning,

usually, from 1D time series as well as for 2D time-frequency spectrograms. CNN models provide advantages such as local dependency, scale invariance, and noise resilience in analytics [11]. However, these models are computationally intensive and power-hungry. This is particularly challenging for low-power embedded applications in the field of Internet-of-Things (IoT).

For ML inference, dedicated hardware architectures are typically used to enhance compute performance and power efficiency. In terms of computational throughput, graphics processing units (GPUs) offer the highest performance; in terms of power efficiency, ASIC and FPGA solutions are more energy efficient [12]. As a result, numerous commercial ASIC and FPGA accelerators have been proposed, targeting both high performance computing (HPC) for data-centers and embedded systems applications.

However, most FPGA accelerators have been implemented to target mid- to high-range FPGAs for computationally

intensive CNN models such as AlexNet, VGG-16, and ResNet-18. The main drawbacks of these implementations are power supply demands, physical dimensions, heat sink requirements, air cooling, and high price. In some cases, these implementations are not feasible for ubiquitous low-power/resource-constrained applications.

To reduce the compute hardware for CNN inference there are two types of research [13]: the first one is deep compression including weight pruning, weight quantization, and compression storage [14], [15]; the second type of research corresponds to a more efficient data representation, also known as custom quantization for dedicated hardware implementation. In this group, hardware implementations with customized 8-bit floating-point computation have been proposed [13], [16], [17]. However, these architectures are inadequate for embedded applications, the target devices are high-end FPGA and PCIe devices.

Reducing the compute hardware with more aggressive quantization such as binary [18], ternary [19], and mixed precision (2-bit activations and ternary weights) [20] typically incur significant accuracy degradation for very low precisions, especially for complex problems [21].

In this paper, we present the Hybrid-Float6 quantization and its dedicated hardware design. In this concept, feature maps are represented by standard 32-bit FP and trainable parameters by 6-bit FP. To preserve accuracy, we introduce a quantization-aware training (QAT) method. To preserve model accuracy, we present a quantization-aware training method, which in some cases improves model performance. For ML compatibility/portability, the 6-bit FP is wrapped into the standard FP representation. The dedicated hardware design extracts the 6-bit format automatically and performs the computation. We propose a parameterized tensor processor implementing a pipelined vector dot-product with HF6. The 6-bit FP representation uses 4-bit exponent and 1-bit mantissa. This approach enables an optimized MAC design by reducing the mantissa multiplication to a mux-adder operation. We leverage the intrinsic error tolerance of ANN to further reduce the hardware design with approximation. This approach reduces latency, resource utilization, and power dissipation. The embedded hardware/software architecture is integrated with TensorFlow Lite using delegate interface to accelerate *Conv2D* tensor operations. We evaluate the applicability of our approach with a CNN-regression model and hardware design exploration for sensor analytics of SHM for anomaly localization. The embedded hardware/software framework is demonstrated on XC7Z007S as the smallest and most inexpensive Zynq SoC device, see Fig. 1. To the best of our knowledge, this is the first research addressing 6-bit floating-point quantization on CNN models and its dedicated hardware design.

Our main contributions are as follows:

- 1) We present the Hybrid-Float6 quantization and its dedicated hardware design. We propose an optimized hardware MAC by reducing the mantissa multiplication to a mux-adder operation. We exploit the intrinsic error

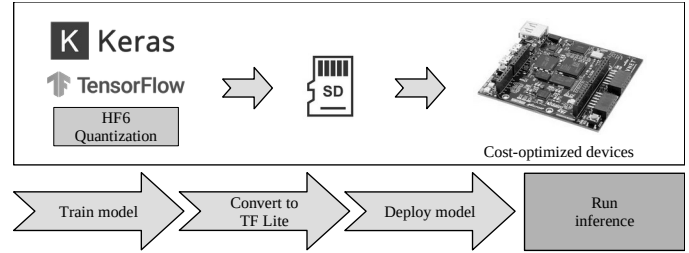


FIGURE 1. The workflow of our approach on embedded FPGAs.

tolerance of ANN to further reduce the hardware design with approximation. To preserve model accuracy, we present a quantization-aware training method, which in some cases improves accuracy.

- 2) We develop a custom hardware/software co-design framework for sensor analytics applications on low-power embedded FPGAs. This architecture integrates TensorFlow Lite.
- 3) We present a customizable tensor processor as a dedicated hardware for HF6. This design computes *Conv2D* tensor operations employing a pipelined vector dot-product with parametrized on-chip memory utilization. The compute engine can be implemented with standard floating-point (with FP Xilinx LogiCORE IPs) and HF6.
- 4) We demonstrate the potential of our approach with a CNN-regression model for anomaly localization in SHM. We address a hardware design exploration. We evaluate inference accuracy, compute performance, hardware resource utilization, and energy consumption.

The rest of the paper is organized as follows. Section II covers the related work; Section III introduces the background for *Conv2D* tensor operation and floating-point number representation; Section IV describes the system design of the hardware/software architecture and the quantized aware training method; Section V presents the experimental results thorough a design exploration flow; Section VI concludes the paper.

This work is available to the community as an open-source project at <https://github.com/YaribNevarez/tensorflow-lite-fpga-delegate.git>.

II. RELATED WORK

In the literature we find plenty of hardware architectures for CNN accelerators implemented in FPGA. Most of the research implements fixed-point quantization, and very limited research focuses on FP. Moreover, to the best of our knowledge, there is no research work exploring FP inference for low-power embedded applications.

A. HYBRID CUSTOM FLOATING-POINT

In [22], Liangzhen Lai et al. proposed a mixed data representation with floating-point for weights and fixed-point for activations. [22] demonstrated on SqueezeNet, AlexNet, GoogLeNet, and VGG-16 that reduced FP quantization (4-

bit exponent and 3-bit mantissa) results in constant negligible accuracy degradation. In [23], Sean O. Settle et al. presented an 8-bit FP quantization scheme, which needs an extra inference batch to compensate for quantization error. However, [22] and [23] did not present a hardware architecture. In [17], Xiacong Lian et al. proposed an accelerator with optimized block floating-point (BFP), in this design the activations and weights are represented by 16-bit and 8-bit FP formats, respectively. This design is demonstrated on Xilinx VC709 evaluation board. This implementation achieves throughput and power efficiency of 760.83 GOP/s and 82.88 GOP/s/W, respectively.

B. LOW-PRECISION FLOATING-POINT

In [16], Chunsheng Mei et al. presented a hardware accelerator for VGG16 model using half-precision FP (16-bit). This design is demonstrated on Xilinx Virtex-7 (XC7VX690T) with PCIe interface. This implementation achieves throughput and power efficiency of 202.8 GFLOP/s and 18.72 GFLOP/s/W, respectively. In [13], Chen Wu et al. proposed a low-precision (8-bit) floating-point (LPFP) quantization method for FPGA-based acceleration. This design is demonstrated on Xilinx Kintex 7 and Ultrascale/Ultrascale+. This implementation achieves throughput and power efficiency of 1086.8 GOP/s and 115.4 GOP/s/W, respectively.

C. LOW-POWER

Two research papers have been reported hardware accelerators targeting XC7Z007S. This is the smallest and most inexpensive device from Zynq-7000 SoC family. In [24], Paolo Meloni et al. presented a CNN inference accelerator for compact and cost-optimized devices. This implementation uses fixed-point for processing light-weight CNN architectures with a power efficiency between 2.49 to 2.98 GOPS/s/W. In [25], Chang Gao et al. presented EdgeDRNN, a recurrent neural network (RNN) accelerator for edge inference. This implementation adopts the spiking neural network (SNN) inspired delta network algorithm to exploit temporal sparsity in RNNs.

III. BACKGROUND

A. CONV2D TENSOR OPERATION

A convolutional layer aims to learn feature representations from an input layer. The convolution layer is made of convolution kernels that are used to compute feature maps. Each unit of a feature map is connected to a region of neighboring units on the input maps (from previous layer). Such a neighborhood of the previous layer is known as the receptive field of the unit. A new feature map can be obtained by first convolving the input maps with a learned kernel and then applying a nonlinear elementwise activation function to the convolved results. All spatial locations on the input maps share a kernel to generate a feature map. All feature maps are obtained by convolving several different kernels [26].

The 2D convolution process is performed by the *Conv2D* tensor operation, described in Eq. (1), where h is the input

feature maps, W is the convolution kernels (known as filters), and b is the bias for the output feature maps [27]. We denote *Conv* as *Conv2D* operator.

$$\text{Conv}(W, h)_{i,j,o} = \sum_{k,l,m}^{K,L,M} h_{(i+k,j+l,m)} W_{(o,k,l,m)} + b_o \quad (1)$$

B. FLOATING-POINT NUMBER REPRESENTATION

The representation of every numerical value, in any number system, is made of an integer and a fractional part. The border that delimits them is called the radix point. The fixed-point format for representing numeric values derives its name from the fact that in this format, the base point is fixed at a certain position. For integer numbers, this position is at the right of the least significant digit.

In scientific computation, it is often necessary to represent very large and very small values. This is difficult to achieve using the fixed-point format because the bit size/width required to maintain both the desired precision and the desired range are very large. In such situations, FP formats are used to represent real numbers. Each FP number can be divided into three fields: sign S , exponent E , and mantissa M . Using the binary number system, it is possible to represent any FP number as:

$$(-1)^S \times 1.M \times 2^{E-B} \quad (2)$$

In FP representations the exponent is biased. This bias depends on the bit size of the exponent field in the particular format. This exponent bias is defined by Eq. (3), where E_{size} is the exponent bit size.

$$B = 2^{E_{size}-1} - 1 \quad (3)$$

There is a natural trade-off between small bit size requiring fewer hardware resources and larger bit size providing higher precision. Within a given total bit size, it is possible to assign various combinations of sizes to the exponent and mantissa fields, with wider exponents resulting in a higher range and wider mantissa resulting in better precision.

The most widely used format for FP arithmetic is the IEEE 754 standard [28]. The IEEE single-precision format (32-bit) is expressed by Eq. (2) with $B = 127$, 8 bits for the exponent and 23 bits for the mantissa, see Fig. 2(a). In FP formats, the numbers are normalized, the leading one is an implicit bit, and only the fractional part is explicitly stored in the mantissa field.

Reduced bit size than those specified in the IEEE 754 standard are often sufficient to provide the desired precision. Reduced designs require fewer hardware resources enabling low-power implementations. In custom hardware designs, it is possible to customize the FP format implemented. In later sections, we use the term *EaMb* to denote FP formats, where a and b are the exponent and mantissa bit size, respectively. For example, E4M1 means 4-bit exponent and 1-bit mantissa, see Fig. 2(d).

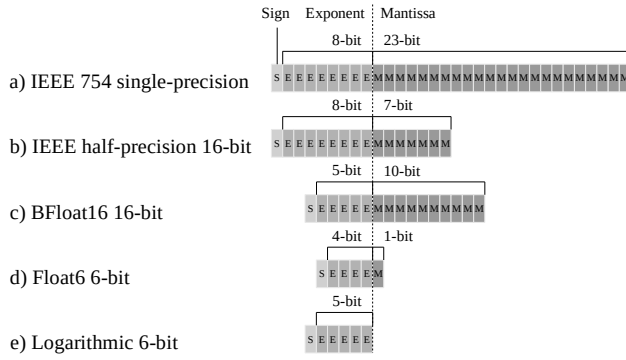


FIGURE 2. Floating-point number representation.

There are three special definitions in IEEE 754 standard. The first is subnormal numbers when $E = 0$, then Eq. (2) is modified to Eq. (4). Infinity and not a number (NaN) are the other two special cases but are not used in our work.

$$(-1)^S \times 0.M \times 2^{1-B} \quad (4)$$

IV. SYSTEM DESIGN

The system design is a hardware/software co-design framework for low-power AI deployment. This architecture allows design exploration of dedicated hardware integrated with TensorFlow Lite on low-cost embedded FPGAs.

A. BASE EMBEDDED SYSTEM ARCHITECTURE

The base embedded system architecture implements a co-operative hardware-software platform. See Fig. 3. The embedded CPU delegates low-level compute-bound tensor operations to the TPs. The TPs employ AXI-Lite interface for configuration and AXI-Stream interfaces via Direct Memory Access (DMA) for data movement from DDR memory. Each TP asserts an interrupt flag once the job/transaction is complete. Interrupt events are handled by the embedded CPU to collect results and start a new transaction. The hardware architecture can vary its resource utilization by customizing the TPs prior to the hardware synthesis.

B. TENSOR PROCESSOR

The TP is a dedicated hardware module to compute tensor operations. This architecture implements high performance communication with AXI-Stream, direct CPU communication with AXI-Lite, and on-chip storage utilizing BRAM. This hardware architecture is implemented with high-level synthesis (HLS). The tensor operations are implemented based on the C++ TensorFlow Lite micro kernels. See Fig. 4.

The TP is an extensible hardware module that executes low-level tensor operations. In this paper, we focus on the *Conv2D* tensor operation that computes 2D convolution layers.

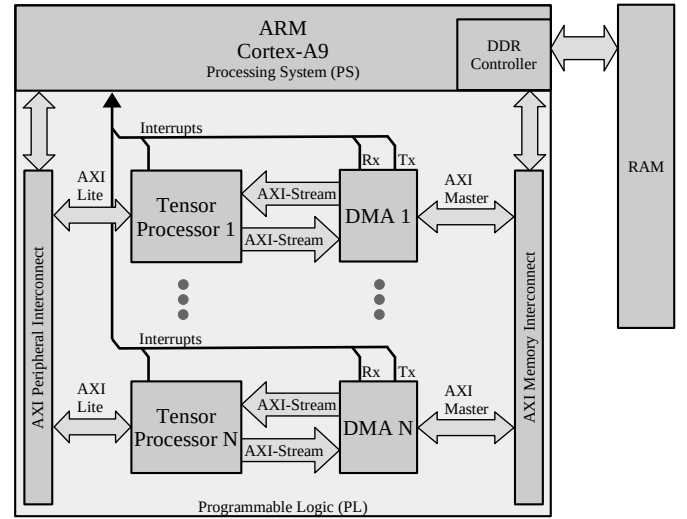


FIGURE 3. Base embedded system architecture.

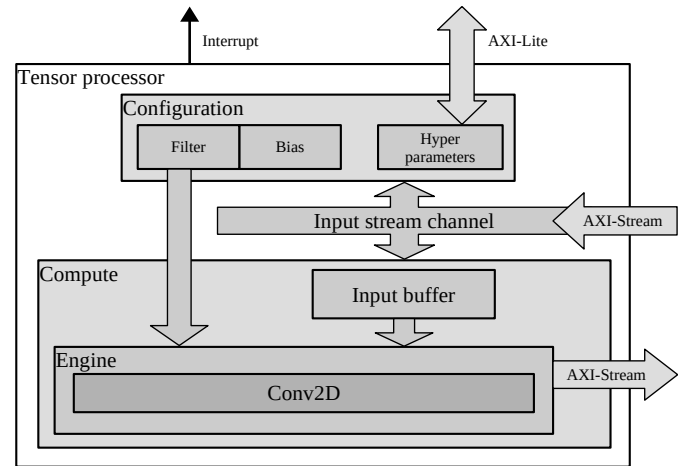


FIGURE 4. Hardware architecture of the proposed tensor processor.

1) Modes of operation

The TP has two modes of operation: *configuration* and *execution*.

- In *configuration* mode, the TP receives the tensor operation hyperparameters: stride, dilation, padding, offset, activation, depth-multiplier, input shape, filter shape, bias shape, and output shape. Afterwards, the TP receives filter and bias tensors, which are locally stored in BRAM. The filter and bias tensors are transferred with standard FP representation. Then, the TP extracts the 6-bit FP format for local on-chip storage.
- In *execution* mode, the TP executes the tensor operation according to the hyperparameters given in the configuration mode. During execution, the input and output tensors are moved from/to the off-chip memory via DMA.

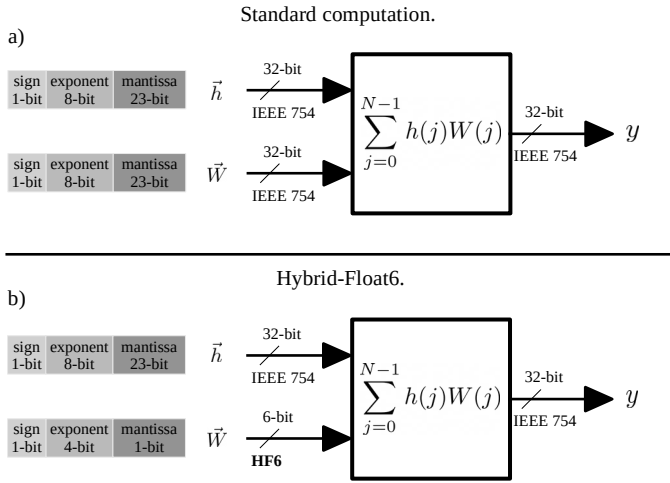


FIGURE 5. Dot-product hardware module with (a) standard floating-point and (b) Hybrid-Float6.

2) Dot-product with hybrid floating-point

We implement the floating-point computation adopting the dot-product with hybrid custom floating-point [29]. The hardware dot-product is illustrated in **Fig. 5** and **Fig. 6(a)**. This design instantiates an HF6 MAC. The accumulator variable is a 64-bit fixed-point number with 23-bit fraction. During operation, the feature map and filter values are extracted from on-chip memory (BRAM). Both values have to be different than zero to enable the MAC operation. The result is biased by accumulating a denormalized bias value, see **Fig. 6(b)**. The ReLu activation is applied and the result is normalized to converted to IEEE 754 standard FP, see **Fig. 6(c)**.

Rather than a parallelized structure, this is a pipelined hardware design suitable for resource-limited devices. The latency in clock cycles of this hardware module is defined by **Eq. (5)**, where N is the vector length. This latency equation is obtained from the general pipelined hardware latency formula: $L = (N - 1)II + IL$, where II is the initiation interval, and IL is the iteration latency. Both II and IL are obtained from the high-level synthesis results. Both the exponent and mantissa bit widths of the filter and bias buffers are set to a 4-bit exponent and a 1-bit mantissa (E4M1), which corresponds to float6 quantization.

$$L_{hf} = N + 7 \quad (5)$$

3) Multiply-Accumulate

The 6-bit FP representation enables hardware a optimization in the mantissa multiplication. The 1-bit mantissa enables efficient multiply-accumulate (MAC) implementations by reducing the mantissa multiplication to a multiplexed addition, see **Fig. 7**. This approach reduces latency, energy consumption, and resource utilization.

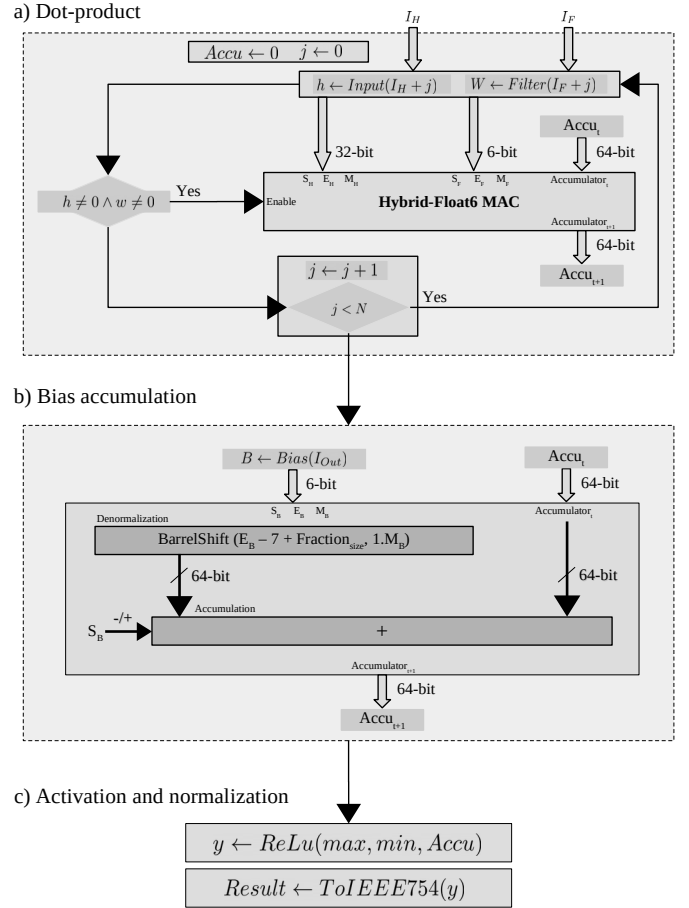


FIGURE 6. (a) Dot-product hardware module with Hybrid-Float6 MAC, (b) bias accumulation, (c) activation and normalization.

The Infinity and NaN special cases are not considered in this design since are not expected in ANN computation. For the subnormal case, the element-wise multiplication is disabled when having a zero entry and applies approximation when having subnormal mantissa. In the case of standard FP, subnormal numbers are not expected and the generated error is negligible. In the case of 6-bit FP, the 1-bit mantissa has one subnormal case, which is handled as a normalized case. This approximation simplifies the hardware design.

The approximation error is defined by the difference between **Eq. (2)** and **Eq. (4)** when $E = 0$ and $M = 2^{-1}$. The result defines the error as $e = 2^{-B-1}$. Then, from **Eq. (3)** with $E_{size} = 4$, we have $B = 7$. Hence, $e = 3.9e-3$. This error is produced when having the subnormal case $E = 0$ and $M = 2^{-1}$, which corresponds to the value $\pm 7.8e-3$ deviated to $\pm 1.17e-2$. This approximation leverages the intrinsic error tolerance of ANN to reduce hardware resource utilization and energy consumption [11].

4) On-chip memory utilization

The total on-chip memory utilization on the TP is defined by **Eq. (6)**, where TP_B and V_M represent the tensor buffers and local variables (memory) required for the design, respec-

Hybrid-Float64 multiply-accumulate

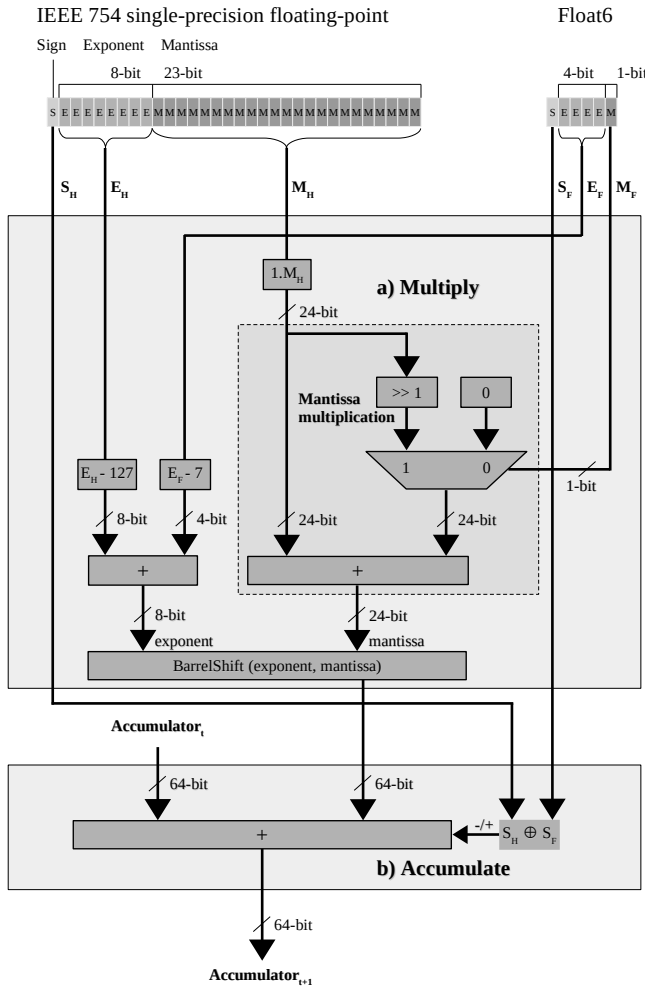


FIGURE 7. Hybrid-Float6 multiply-accumulate hardware design.

tively. **Eq. (7)** defines the tensor buffers, where $Input_M$ is the *input buffer*, $Filter_M$ is the *filter buffer*, $Bias_M$ is the *bias buffer*. The on-chip memory buffers are defined in bits. **Fig. 8** illustrates the convolution operation utilizing the on-chip memory buffers.

$$TP_M = TP_B + V_M \quad (6)$$

$$TP_B = Input_M + Filter_M + Bias_M \quad (7)$$

The memory utilization of *input buffer* is defined by **Eq. (8)**, where K_H is the height of the convolution kernel, W_I is the width of the input tensor, C_I is the number of input channels, and $BitSize_{I_I}$ is the bit size of input tensor.

$$Input_M = K_H W_I C_I BitSize_I \quad (8)$$

The memory utilization of *filter buffer* is defined by **Eq. (9)**, where K_W and K_H are the width and height of the convolution kernel, respectively; C_I and C_O are the number

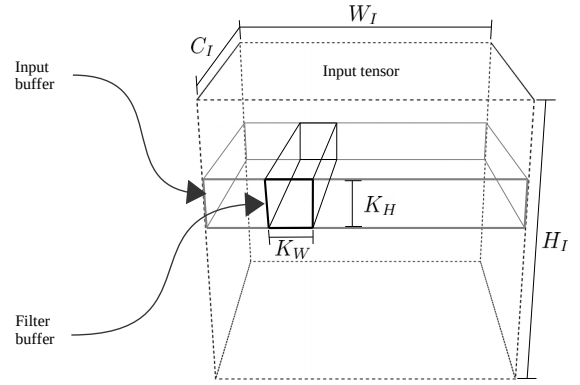


FIGURE 8. Design parameters for on-chip memory buffers on the TP.

of input and output channels, respectively; and $BitSize_F$ is the bit size of filter values.

$$Filter_M = C_I K_W K_H C_O BitSize_F \quad (9)$$

The memory utilization of *bias buffer* is defined by **Eq.** (10), where C_O is the number of output channels, and $BitSize_B$ is the bit size of bias values.

$$Bias_M = C_O BitSize_B \quad (10)$$

As a design trade-off, **Eq.** (11) defines the capacity of output channels based on the given design parameters. The total on-chip memory TP_M determines the TP capacity.

$$C_O = \frac{TP_M - V_M - K_H W_I C_I BitSize_I}{C_I K_W K_H BitSize_F + BitSize_B} \quad (11)$$

The floating-point formats implemented in the TP are defined by $BitSize_F$, $BitSize_B$ and $BitSize_I$. The HF6 defines 6-bit for $BitSize_F$ and $BitSize_B$, and 32-bit for $BitSize_I$. These are design parameters defined before hardware synthesis. This allows fine control of BRAM utilization, which is suitable for resource-limited devices.

C. TRAINING METHOD

The models are trained and quantized in separate stages.

1) Training with Iterative Early Stop

To achieve better performance on CNN-regression models, we implement a training procedure with iterative early stop cycle. This allows to reach better local minima. This is a four steps process:

- 1) A model is obtained with an initial training with standard early stop monitoring.
- 2) The model is iteratively re-trained with standard early stop to search for better local minima. In each early stop the Adam optimizer restarts the moving averages.
- 3) In case of a better local minimum, the base model is updated/saved and used for subsequent re-training iterations, otherwise it is discarded.
- 4) The cyclic process stops automatically with a given patience. This allows to set a maximum training iterations before the stop.

This method is described in **Algorithm 1**.

2) Quantization Aware Training

The quantization aware training (QAT) method is integrated into the training process, this operates after each mini-batch update. The quantization is applied on the trainable parameters of convolution layers. This method is implemented as a callback function in the TensorFlow/Keras framework, see **Algorithm 2**.

The quantization method uses rounding strategy to reduce the FP representation. This maps the full precision FP values to the closest representable 6-bit FP values, see **Algorithm 3**. This method quantizes the filter and bias tensors of the convolution layers. We have observed that the exponent bit size plays a more predominant influence on the model accuracy than the mantissa bit size. In [22], Lai et al. demonstrated that 4-bit exponent is adequate and consistent across different networks (SqueezeNet, AlexNet, GoogLeNet, VGG-16). In this work, we investigate 4-bit exponent and 1-bit mantissa.

Algorithm 1: Training with iterative early stop cycle.

```

input:  $MODEL$  as the input model.
input:  $D_{train}$  as the training data set.
input:  $D_{val}$  as the validation data set.
input:  $N_I$  as the stop patience for iterative training cycle.
input:  $N_E$  as the early stop patience (epochs) for training.
input:  $B_{size}$  as the mini-batch size.
output:  $MODEL$  as the full-precision output model.
 $Train(MODEL, D_{train}, D_{val}, N_E, B_{size})$ 
 $mse_i \leftarrow Evaluate(MODEL, D_{val})$  // Benchmark
 $n_i \leftarrow 0$ 
while  $n_I < N_I$  do
  // Iterative early stop cycle
   $Train(MODEL, D_{train}, D_{val}, N_E, B_{size})$ 
   $mse_v \leftarrow Evaluate(MODEL, D_{val})$ 
  if  $mse_v < mse_i$  then
     $Update(MODEL)$ 
     $mse_i \leftarrow mse_v$ 
  else
     $MODEL \leftarrow LoadPreviousModel()$ 
     $n_I \leftarrow n_I + 1$ 
  end if
end while

```

D. EMBEDDED SOFTWARE ARCHITECTURE

The software architecture is a layered object-oriented application framework written in C++, see **Fig. 9**. A description of the software layers is as follows:

- **Application:** As the highest level of abstraction, this software layer implements the application invoking the ML library.
- **Machine learning library:** This layer consist of TensorFlow Lite for micro controllers. This offers a comprehensive high level API that allows ML inference.

Algorithm 2: OnMiniBatchUpdate_Callback.

```

input:  $MODEL$  as the full-precision input model.
input:  $E_{size}$  as the target exponent bits size.
input:  $M_{size}$  as the target mantissa bits size.
input:  $D_{train}$  as the training data set.
input:  $D_{val}$  as the validation data set.
input:  $N_{ep}$  as the number of epochs.
input:  $B_{size}$  as the mini-batch size.
output:  $MODEL$  as the quantized output model.
//Quantize
 $MODEL \leftarrow Algorithm\ 3(MODEL, E_{size}, M_{size})$ 
if  $1 < epoch$  then
  // Update model after first epoch
   $mse_v \leftarrow Evaluate(MODEL, D_{val})$ 
  if  $mse_v < mse_i$  then
     $Update(MODEL)$ 
     $mse_i \leftarrow mse_v$ 
  end if
end if

```

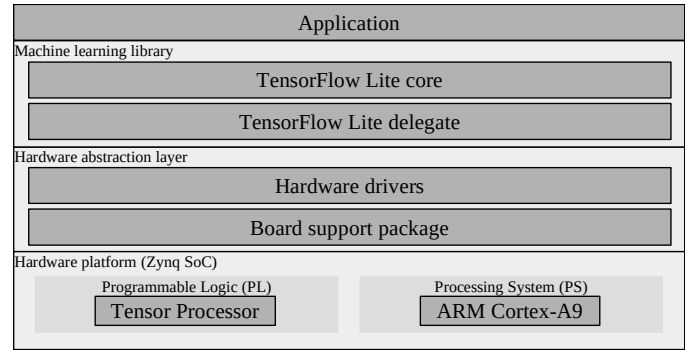


FIGURE 9. Base embedded software architecture.

This provides delegate software interfaces for custom hardware accelerators.

- **Hardware abstraction layer:** This layer consist of the hardware drivers to handle initialization and runtime operation of the TP and DMA.

V. EXPERIMENTAL RESULTS

In this section, we present experimental results on a low-power/low-cost sensor analytics application. As a use case, we present a CNN-regression model to predict x- y- coordinates of structural anomalies based on acoustic sensor data. We compare quantitative and qualitative aspects of the analytics using floating-point 32-bit, fixed-point 8-bit, Hybrid-Logarithmic 6-bit, and Hybrid-Float6.

To demonstrate the proposed hardware concept, we deploy the CNN model for low-power inference in the smallest Zynq SoC. We compare the performance of the TP implemented with standard FP (using Xilinx LogiCORE IPs) and Hybrid-Float6 architecture.

Algorithm 3: Custom floating-point quantization.

input: $MODEL$ as the CNN.
input: E_{size} as the target exponent bit size.
input: M_{size} as the target mantissa bits size.
input: $STDM_{size}$ as the IEEE 754 mantissa bit size.
output: $MODEL$ as the quantized CNN.

for $layer$ in $MODEL$ **do**
 if $layer$ is *Conv2D* or *SeparableConv2D* **then**
 $filter, bias \leftarrow GetWeights(layer)$
 for x in $filter$ and $bias$ **do**
 $sign \leftarrow GetSign(x)$
 $exp \leftarrow GetExponent(x)$
 $fullexp \leftarrow 2^{E_{size}-1} - 1$ // Get full range value
 $cman \leftarrow GetCustomMantissa(x, M_{size})$
 $leftman \leftarrow GetLeftoverMantissa(x, M_{size})$
 if $exp < -fullexp$ **then**
 $x \leftarrow 0$
 else if $exp > fullexp$ **then**
 $x \leftarrow (-1)^{sign} \cdot 2^{fullexp} \cdot (1 + (1 - 2^{-M_{size}}))$
 else
 if $2^{STDM_{size}-M_{size}-1} - 1 < leftman$ **then**
 $cman \leftarrow cman + 1$ // Above halfway
 if $2^{M_{size}} - 1 < cman$ **then**
 $cman \leftarrow 0$ // Correct mantissa overflow
 $exp \leftarrow exp + 1$
 end if
 end if
 // Build custom quantized floating-point value
 $x \leftarrow (-1)^{sign} \cdot 2^{exp} \cdot (1 + cman \cdot 2^{-M_{size}})$
 end if
 end for
 $SetWeights(layer, filter, bias)$
 end if
end for

A. SENSOR ANALYTICS APPLICATION

The analytics model is designed to predict x- y- coordinates of acoustic emissions on a metal plate. The metal plate is in the presence of noise disturbance to simulate realistic conditions. In this subsection, we present the structure for experimental setup, data sets, and the CNN-regression model.

1) Experimental Setup

The experiment uses eight piezoelectric sensors (Vallen Systeme VS900) fixed on a metal plate (90 cm x 86.6 cm x 0.3 cm). The VS900 devices can operate either in active or passive mode. Six VS900 are used in passive mode as acoustic sensors and two in active mode to produce acoustic emissions. These acoustic emissions simulate anomalies on x- y- coordinates as well as the noise disturbance on the system. See Fig. 10(a). The acoustic emissions are labeled with their coordinates to create data sets.

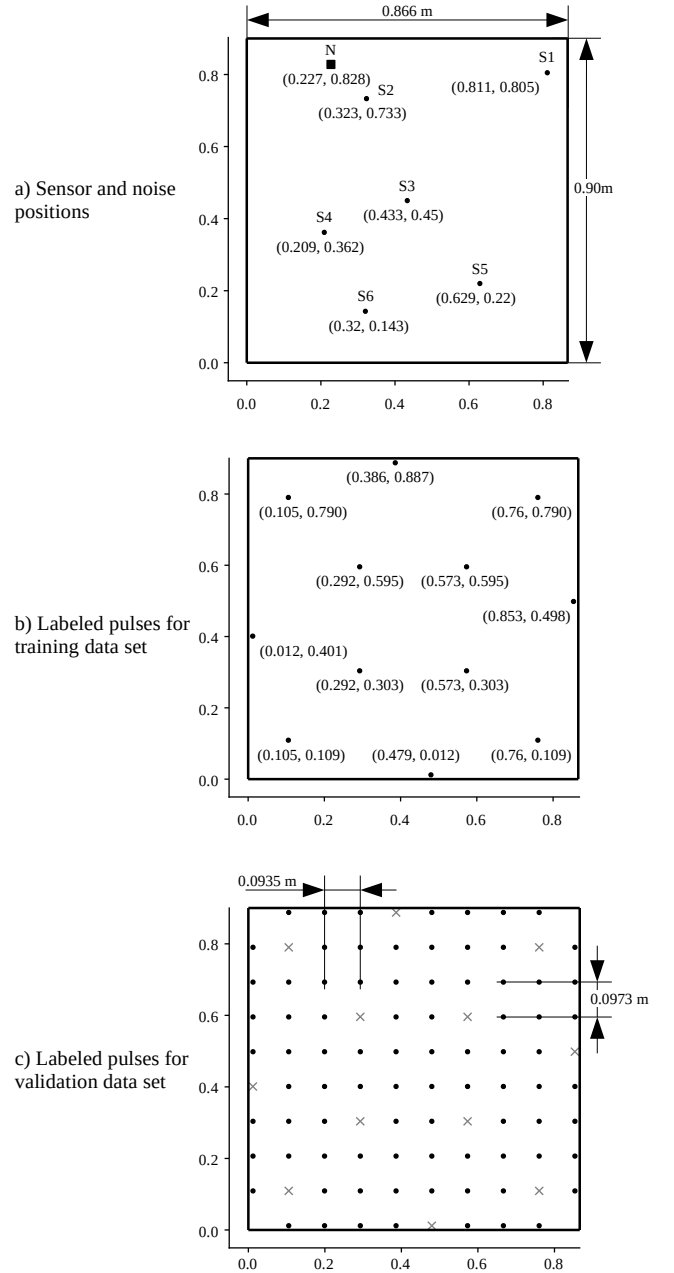


FIGURE 10. Experimental setup for sensor analytics on structural health monitoring.

2) Data Sets

The data sets are recorded applying pulses on the metal plate, the x- y- coordinates of these pulses are used as labels. The pulses for training and validation data sets are shown in Fig. 10(b) and Fig. 10(c), respectively. The pulses for training and validation data sets are mutually exclusive, this exclusion is represented by the cross symbols in Fig. 10(c). This creates a grid layout used to collect samples for the data sets. This grid is 10 x 10. This grid does not consider the four corners as they are used for structure holders.

In order to create reproducible acoustic emissions, we

use 9-cycle sine pulse in a Hanning window with central frequency f_c (narrow-banded in the frequency domain). We assume guided Lamb waves based on the plate structure. The narrow-band behavior also reduces the dispersion of the acoustic emission waves [30]. The waveform can be expressed as a function of time t as follows:

$$x_{\text{pulse}}(t) = \frac{1}{2} \left(1 - \cos \frac{f_c t}{5} \right) A_0 \sin f_c t. \quad (12)$$

To generate the data sets, we use slightly different pulse amplitudes and frequencies for excitation. The pulse frequency f_c is varied in 1 kHz steps between 300 kHz and 349 kHz and the amplitude A_0 is varied in 0.1 V steps between 2.6 V and 3.5 V. This results in 500 different pulses for each of the excitation points.

The signals for labeled pulses and noise disturbance are generated by arbitrary waveform generators (AWGs). The sensor signals are recorded via a Vallen AMSY-6 measurement system with a resolution of 18 bits and a sampling rate of $f_s = 10 \text{ MHz}$. The disturbance signal is gaussian noise with amplitudes between 0-3 V. This noise is applied via the piezoelectric device N at $x = 0.227$ and $y = 0.828$, see Fig. 10(a).

To obtain both time and frequency domain information, the sampled pulses are converted into the time-frequency domain using the Short-Time Fourier Transform (STFT). This is calculated as follows [31]:

$$\mathcal{F}_{m,k}^\gamma = \sum_{n=0}^{N-1} x[n] \cdot \gamma^*[n - m\Delta M] \cdot e^{\frac{-j2\pi kn}{N}} \quad (13)$$

Here $x[n]$ describes a discrete-time signal and $\gamma^*[n - m\Delta M] \cdot e^{\frac{-j2\pi kn}{N}}$ the time- and frequency-shifted window function inside the considered interval $[0, N - 1]$. ΔM describes the time shift and N the transformation window. Since only discrete frequencies and time points are considered, $m = 0, 1, \dots, M - 1$ is valid. This complex-valued STFT is converted to real numbers via the magnitude square for pictorial representation in a spectrogram $\mathcal{S}_{m,k}$:

$$\mathcal{S}_{m,k} = \left| \mathcal{F}_{m,k}^\gamma \right|^2 = \left| \sum_{n=0}^{N-1} x[n] \cdot \gamma^*[n - m\Delta M] \cdot e^{\frac{-j2\pi kn}{N}} \right|^2 \quad (14)$$

In addition, these spectrograms are scaled in decibels. The spectrogram in decibels $\mathcal{S}_{m,k,\text{dB}}$ results in $\mathcal{S}_{m,k,\text{dB}} = 20 \cdot \log_{10}(\mathcal{S}_{m,k})$. For the conversion of the data, we use a signal length of 400 μs (75 μs pretrigger and 325 μs post trigger). Thus, the arrival times of the pulses are included in the spectrogram for all channels and labeled positions. We use a Blackman window function [32], a Fast Fourier Transform (FFT) length of 32 samples, and an overlap of 8 samples. The spectrograms are calculated for frequencies in the range of 100 kHz to 500 kHz. This results in a spectrogram with 8x16 values (8 frequency values, 16 time values).

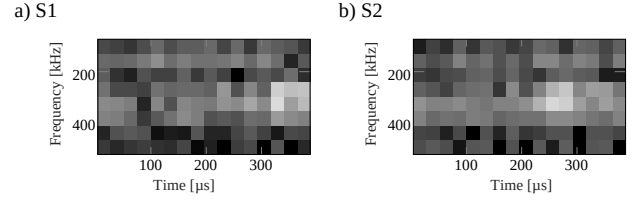


FIGURE 11. Spectrograms of sensors S_1 , S_2 converted to grayscale for pulses at $x = 0.105$, $y = 0.109$ with noise disturbance.

In order to generate larger data sets, we create four further variants with time shifts of 15 μs / 30 μs / 45 μs / 60 μs . Subsequently, all spectrograms are converted to grayscale with scaling between -100dB and -40dB, see Fig. 11. Overall, the data set has a size of 500 (pulses) \cdot 5 (spectrograms) \cdot 6 (listening sensors) \cdot 96 (excitation points) = 1,440,000 images.

3) CNN-Regression Model

The data analytics is implemented with a CNN-regression model, see Fig. 12. The structure of the model is described below:

- Input tensor.** This is composed of spectrograms from the sensor signals. The tensor shape is defined by $S \times T \times F$, where S is the number of sensors, and $T \times F$ is the time-frequency resolution of the spectrograms, see Fig. 12(a).
- Feature extraction.** This is composed of three blocks of convolution, batch normalization, and max-pooling layers, see Fig. 12(b). The number of channels in the convolution layers are defined by the hyper-parameters A , B , and C .
- Regression function.** This is an arbitrary function implemented with two fully connected layers and an output layer with linear activation, see Fig. 12(c).

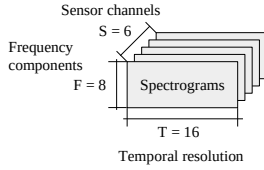
B. TRAINING

1) Base Model

The model in Fig. 12 is trained using Adam algorithm with iterative early stop. The Adam optimizer is configured with the default settings presented in [33]: $\alpha = 0.001$, $\beta_1 = 0.9$, $\beta_2 = 0.999$, and $\epsilon = 1e-8$. The training cycle patience is 10 iterations, the optimizer is executed with early stop patience of 10 epochs, and mini-batch size of 512 samples. This is applied using the method described in Algorithm 1 with $N_I = 10$, $N_E = 10$, $B_{\text{size}} = 512$.

The training results are illustrated in Fig. 13(a). In this experiment, the initial and the final models achieve $MSE = 0.0135m^2$ and $MSE = 0.0122m^2$, respectively. The MSE is calculated with the Euclidean distance (loss) between the expected and the predicted coordinates. The initial model is obtained at the first early stop. In each stop, the moving averages of the Adam optimizer get initialized. This facilitates searching for better local minima. The model gets saved/updated when finding a better minimum.

a) Input tensor



CNN-regression model

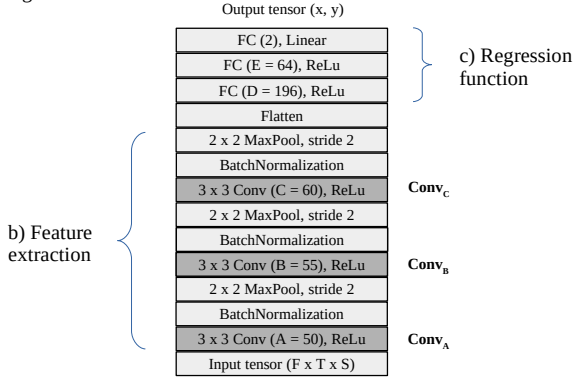


FIGURE 12. CNN-regression model for sensor analytics.

The resulting model achieves $MSE = 0.0122m^2$, which corresponds to $MAE = 0.0955m$. See Fig. 14(a). In total, the training takes 379 epochs in 25 stops. The first stop takes 43 epochs for the initial model and subsequent training iterations take an average of 14 epochs. The total time is 53 minutes using a PC with AMD Ryzen 5 5600H and NVIDIA GeForce RTX 3050.

2) TensorFlow Lite 8-bit quantization

This integer quantization is an optimization method that converts 32-bit FP numbers (such as weights and activations) to 8-bit fixed-point numbers. This quantization scheme allows inference to be carried out using integer-only arithmetic [30].

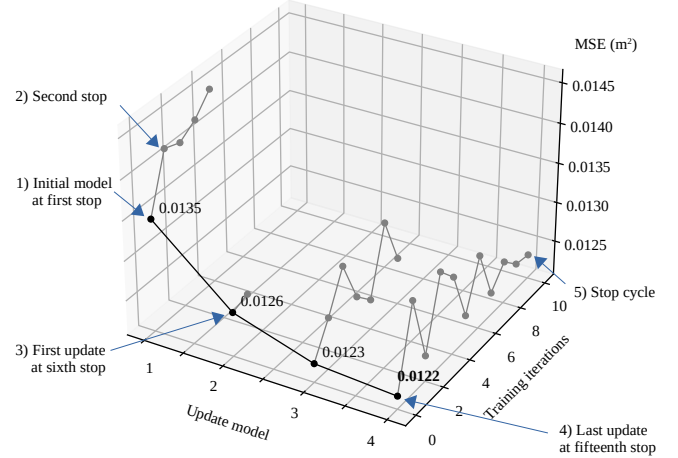
The base model is quantized using the TensorFlow Lite library with integer-only quantization settings. The filter and bias tensors are represented by 8-bit and 32-bit signed integers, respectively. The input and output activation tensors are represented by 8-bit signed integer. For convolution layers, this quantization includes two additional tensor coefficients (output-multiplier and output-shift). These tensors are the same shape as the bias tensor and represented by 32-bit signed integers as well.

The fixed-point model achieves $MSE = 0.0122m^2$ and $MAE = 0.0952m$. See Fig. 14(b). The MAE obtains a reduction of 0.31% compared to the base model. We attribute this to the regularization effect.

3) Quantization Aware Training for Hybrid-Float6

The QAT is a post-training step. We run this method during two epochs with mini-batch size of 10 samples with 4-bit exponent and 1-bit mantissa as parameters. This is applied

a) Training with iterative early stop.



b) Quantization aware training

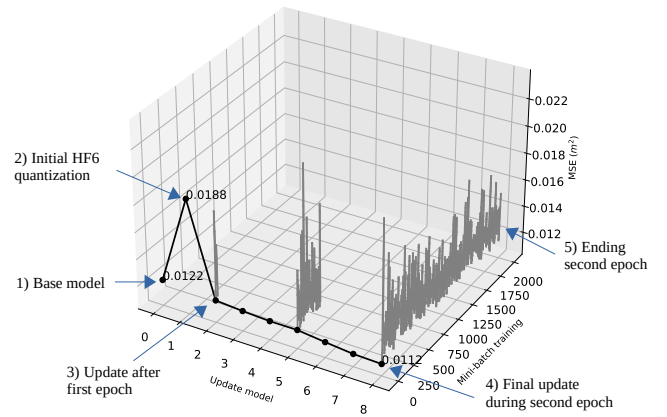


FIGURE 13. Training results.

using the method described in Algorithm 2 with $N_{ep} = 2$, $B_{size} = 10$, $E_{size} = 4$, $M_{size} = 1$.

The QAT is illustrated in Fig. 13(b). First, the model gets quantized with HF6 format before starting QAT, this obtains $MSE = 0.0188m^2$ and $MAE = 0.1232m$. This illustrates the inference of the base FP model (without QAT) on HF6 hardware. See Fig. 14(c). Then, after QAT, the final model achieves $MSE = 0.0112$ and $MAE = 0.0919$. This corresponds to an error reduction of 8.2% and 3.77%, respectively. See Fig. 14(d). The QAT time is 185 minutes.

4) Quantization Aware Training for Hybrid-Logarithmic 6-bit

For the sake of quality comparison, we generate the model with 6-bit logarithmic quantization on convolution parameters, see Fig. 2(e). This quantization matches the bit size of HF6. We run the QAT on the base model with hybrid logarithmic parameters. Then, the filter and bias tensors of convolution layers are represented by 6-bit signed logarithmic. This is applied using the method described in Algorithm 2 with $N_{ep} = 2$, $B_{size} = 10$, $E_{size} = 5$, $M_{size} = 0$.

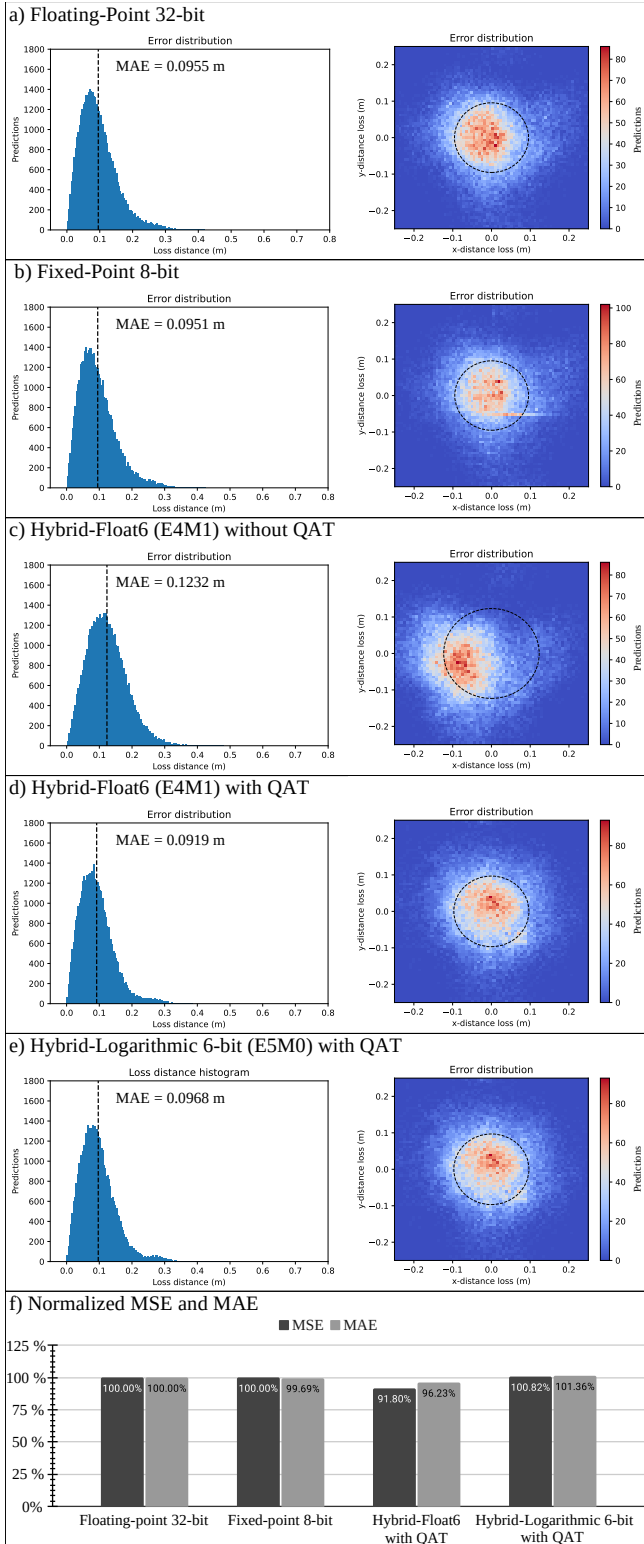


FIGURE 14. Performance of the model with different data representations.

In this case, the model gets quality degradation. The model reaches $MSE = 0.0123$ and $MAE = 0.0968$, which correspond to an error increase of 0.82% and 1.36%, respectively.

See Fig. 14(e).

A summary of inference with different data representations is presented in Fig. 14(f).

C. HARDWARE DESIGN EXPLORATION

The proposed hardware/software co-design is demonstrated on the Zynq-7007S system-on-chip (SoC) on the MiniZed development board. This SoC integrates a single ARM Cortex-A9 processing system (PS) and a programmable logic (PL) equivalent to Xilinx Artix-7 (FPGA) in a single chip [34]. The Zynq-7007S SoC architecture maps the custom logic and software in the PL and PS, respectively.

In this platform, we implement the proposed hardware/software architecture to deploy the sensor analytics application. The desired model is converted to TensorFlow Lite (floating-point) and deployed on the SoC as a hex dump in a C array, this is used for the embedded software build. The Zynq-7007S SoC performs inference running TensorFlow Lite on the PS. The computational workload of convolution layers is delegated to the dedicated hardware.

1) Benchmark on Embedded CPU

We explore the performance of the embedded CPU for inference without hardware acceleration. In this case, TensorFlow Lite creates the CNN as a sequential model that allocates all computation to the CPU (ARM Cortex-A9) at 666 MHz and power dissipation of 1,187W.

The compute performance and run-time inference of the CPU are shown in Tab. 2(a) and Fig. 16(a), respectively.

2) Benchmark on Tensor Processor with Standard Floating-Point Hardware using Xilinx LogiCORE IP

For this design, we implement the TP with standard FP hardware prior synthesis. The design parameters are:

- Max convolution kernel size: $K_W = K_H = 3$.
- Max input tensor width: $W_I = 16$.
- Max input and output channels: $C_I = 55$, $C_O = 60$.
- Filter and bias bit size: $BitSize_F = BitSize_B = 32$.
- Input tensor bit size: $BitSize_I = 32$.

Using equations from Section IV-B4, the on-chip memory buffer utilization are $Input_M = 84,480b$, $Filter_M = 950,400b$, and $Bias_M = 1,920b$. Hence, the required on-chip memory buffer size is $TP_B = 1,036,800b$.

The post-implementation resource utilization and power dissipation are presented in Tab. 1(a). The complete hardware platform utilizes 83% of BRAM, this includes the on-chip memory requirements of the TP, DMA, and AXI interconnects. The total available on-chip memory (BRAM) on the Zynq-7007S SoC is 1.8Mb. The estimated power dissipation of the TP is 85mW at 200MHz (this estimation is provided by Xilinx Vivado).

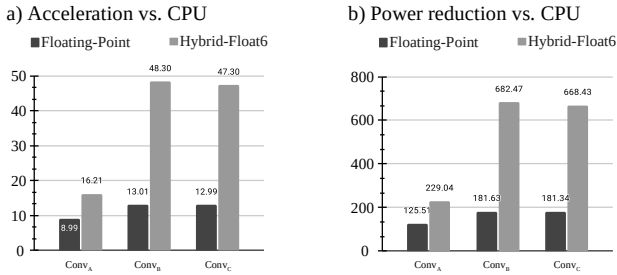
The compute performance and inference schedule of the model on this hardware implementation are shown in Tab. 2(b) and Fig. 16(b), respectively. In this implementation, TensorFlow Lite delegates computation of $Conv2D$ tensor operations to the TP.

TABLE 1. Resource utilization and power dissipation on the Zynq-7007S SoC.

| TP engine | Post-implementation resource utilization | | | | Power (W) |
|--------------------|--|---------------|-----------|--------------------|-----------|
| | LUT | FF | DSP | BRAM 36Kb | |
| (a) Floating-Point | 5,578 39% | 8,942 31% | 23 35% | 41.5 83% | 1.429 |
| (b) Hybrid-Float6 | 7,313 51% | 10,330 36% | 20 30% | 15 30% | 1.424 |

TABLE 2. Compute performance of the CPU and TP on each Conv2D tensor operation. This table presents: tensor operation, computational cost in mega floating-point operations (MFLOP), latency, throughput, power efficiency, and estimated energy consumption as the energy delay product (EDP).

| Operation | MFLOP | t (ms) | MFLOP/s | MFLOP/s/W | EDP (mJ) |
|---|-------|--------|---------|-----------|----------|
| a) CPU (ARM Cortex-A9) @666MHz, 1.187 W | | | | | |
| Conv _A | 0.691 | 112.24 | 6.16 | 5.19 | 133.23 |
| Conv _B | 1.584 | 213.13 | 7.43 | 6.26 | 252.99 |
| Conv _C | 0.475 | 46.59 | 10.20 | 8.59 | 55.31 |
| b) TP (Floating-Point engine) @200MHz, 85 mW | | | | | |
| Conv _A | 0.691 | 12.49 | 55.34 | 651.11 | 1.06 |
| Conv _B | 1.584 | 16.39 | 96.66 | 1,137.20 | 1.39 |
| Conv _C | 0.475 | 3.59 | 132.44 | 1,558.13 | 0.30 |
| c) TP (Hybrid-Float6 engine) @200MHz, 84 mW | | | | | |
| Conv _A | 0.691 | 6.92 | 99.81 | 1,188.24 | 0.58 |
| Conv _B | 1.584 | 4.41 | 358.94 | 4,273.09 | 0.37 |
| Conv _C | 0.475 | 0.99 | 482.44 | 5,743.29 | 0.08 |

**FIGURE 15.** Inference acceleration and power reduction on the TP with floating-point and HF6 vs. CPU on the Zynq-7007S SoC.

The implementation of the dot-product with standard FP engine (IEEE 754 arithmetic) utilizes proprietary multiplier and adder FP operator cores. Vivado HLS implements FP arithmetic operations by mapping them onto Xilinx LogiCORE IP cores, these FP operator cores are instantiated in the resultant RTL [35]. In this case, the implementation of the dot-product with the standard FP computation reuses the multiplier and adder cores in different compute sections of the TP. The post-implementation resource utilization and power dissipation of the floating-point operator cores are shown in **Tab. 3**.

TABLE 3. Resource utilization and power dissipation of multiplier and adder floating-point (IEEE 754) operator cores (Xilinx LogiCORE IP).

| Core operation | DSP | FF | LUT | Latency (clk) | Power (mW) |
|----------------|-----|-----|-----|---------------|------------|
| Multiplier | 3 | 151 | 325 | 4 | 7 |
| Adder | 2 | 324 | 424 | 8 | 6 |

3) Tensor Processor with Hybrid-Float6 Hardware

To demonstrate the proposed design, the TP with HF6 hardware restates the standard FP design parameters with the following customization for the FP 6-bit quantization in filter and bias: $BitSize_F = BitSize_B = 6$.

Using equations from Section IV-B4, the on-chip memory requirements are $Input_M = 84,480b$, $Filter_M = 178,200b$, $Bias_M = 360b$. Hence, the required on-chip memory buffer size is $TP_B = 263,040b$.

The post-implementation resource utilization and power dissipation are presented in **Tab. 1(b)**. The complete hardware platform utilizes 30% of BRAM, this includes the on-chip memory requirements of the TP, DMA, and AXI interconnects. The estimated power dissipation of the TP is $84mW$ at $200MHz$ (this estimation is provided by Xilinx Vivado).

The compute performance and inference schedule of the model on this hardware implementation are shown in **Tab. 2(c)** and **Fig. 16(c)**, respectively. **Fig. 15** presents a comparison of the acceleration and the reduction of power dissipation between standard FP and HF6 hardware implementations.

This deployment does not require model parameter extraction/treatment. The 6-bit FP representation is wrapped into the standard FP. The dedicated hardware design extracts the 6-bit format automatically and performs computation.

D. DISCUSSION

1) Training and Quantization

The training with iterative early stop obtains a model with enhanced accuracy than standard early stop. This method iteratively resets the moving averages of Adam's optimizer, which helps to find better local minima. This iterative search is suitable for models with low computational cost.

The TensorFlow Lite 8-bit quantization preserves the overall model accuracy. In some cases, the associated regularization effect can improve the accuracy. However, the error distribution in CNN linear regressions gets slightly degraded. **Fig. 17(b)** shows this effect on three different models, where vertical and horizontal patterns appear in the error distribution of fixed-point quantization. We attribute this effect to the 8-bit resolution in the activation maps. In the case of HF6 quantization, the activation maps are represented by FP preventing this degradation.

The proposed 6-bit FP representation (E4M1) in convolution parameters improves latency, hardware area, and power dissipation, while preserving model accuracy. In our application, this number format produces better results than the 6-bit logarithmic representation (E5M0). This is demonstrated in **Fig. 14(d)** and **Fig. 14(e)**.

Applying HF6 quantization on ALL-CNN-C [36] produces an accuracy degradation of 1.39% and 0.11% with QAT. While applying 6-bit logarithmic produces a degradation of 11.18% and 7.22% with QAT.

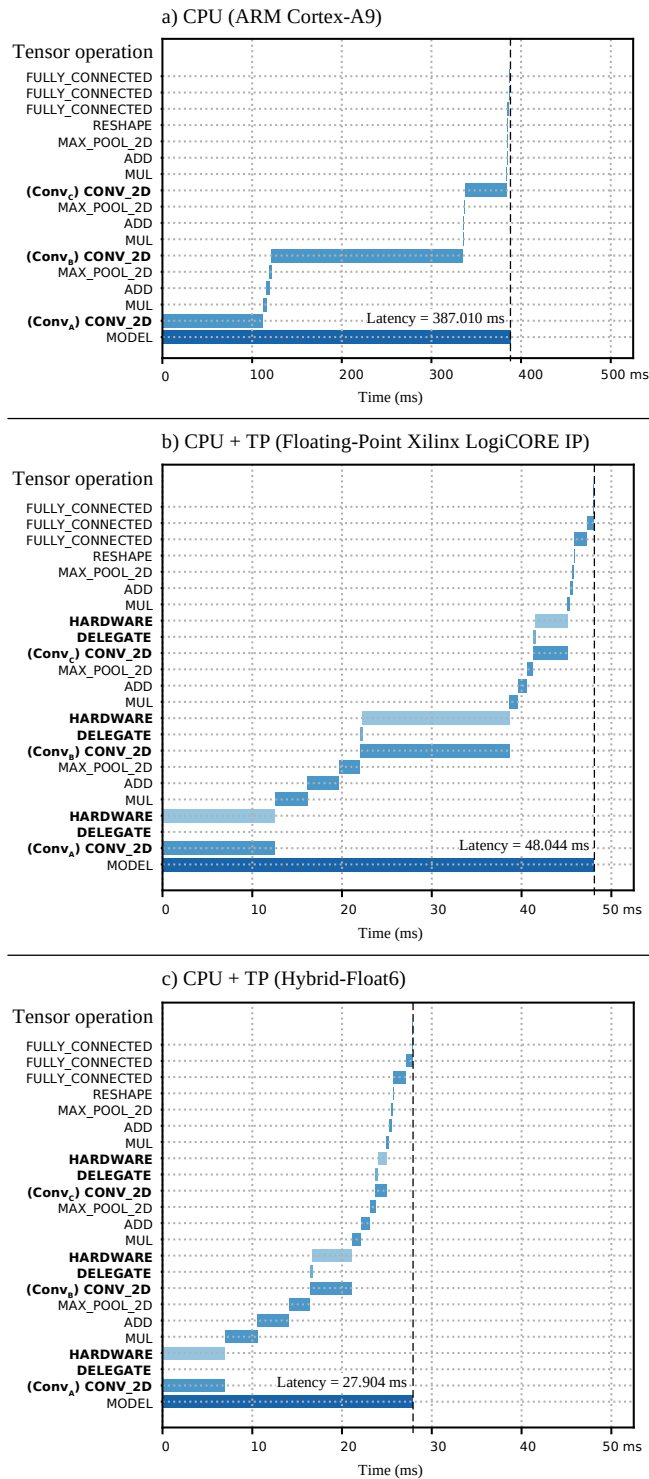


FIGURE 16. Run-time inference of TensorFlow Lite on the Zynq-7007S SoC. (a) CPU ARM Cortex-A9 at 666MHz, (b) cooperative CPU + TP with floating-point Xilinx LogiCORE IP at 200MHz, and (c) cooperative CPU + TP with Hybrid-Float6 at 200MHz.

2) Implementation and Performance

The proposed HF6 hardware design reduces on-chip memory and DSP utilization while slightly increasing FF and LUT compared to the standard FP hardware implementation. See

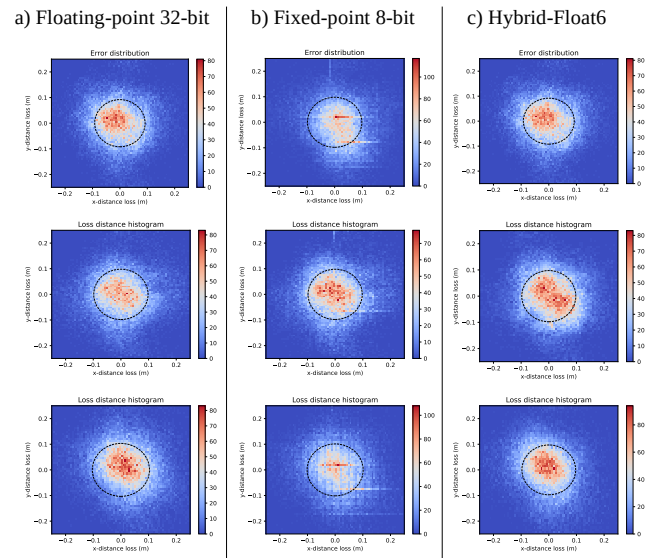


FIGURE 17. 2D error distribution of three CNN-regression models.

Tab. 1 and **Fig. 18**. The HF6 hardware is implemented using FF and LUT, while the FP hardware is implemented using Xilinx LogiCORE IPs with DSPs.

The compute performance of the CPU and TP on each convolution layer of the model is presented in **Tab. 2** and **Fig. 15**. The peak acceleration and power efficiency of the TP with standard FP is $13\times$ and 1,558.13 MFLOPS/s/W, respectively. The peak acceleration and power efficiency of the TP with HF6 is $48.3\times$ and 5,743.29 MFLOPS/s/W, respectively. The HF6 hardware demonstrates an improvement of $3.7\times$ in acceleration and power efficiency with respect to the standard FP hardware. See **Fig. 15**. The estimated power dissipation on the SoC is presented in **Fig. 19**. This shows a very similar breakdown of power dissipation in both implementations. However, the energy efficiency is increased due to the reduced latency in HF6 hardware. A comparison of related work is presented in **Tab. 4**.

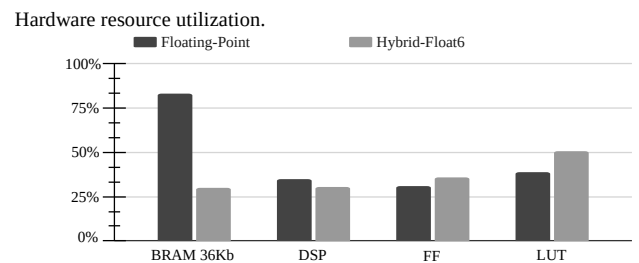


FIGURE 18. Hardware resource utilization on the Zynq-7007S SoC.

The run-time inference of TensorFlow Lite on the SoC is illustrated in **Fig. 16**. This shows a cooperative system where the convolution operations are delegated to the dedicated hardware accelerator. The ARM CPU obtains a latency of 387ms (2.58 FPS). The platform with standard FP hardware

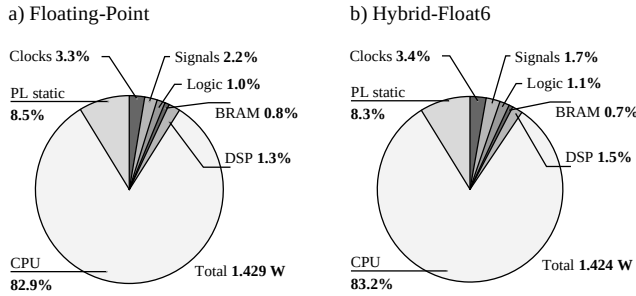


FIGURE 19. Estimated power dissipation on the Zynq-7007S SoC with PS at 666MHz and PL at 200MHz.

obtains a latency of 48ms (20.8 FPS), while the implementation with HF6 obtains a latency of 27.9ms (35.84 FPS). These represent an overall acceleration of 8× and 13.87× over the CPU, respectively.

For ML compatibility/portability, the 6-bit FP is wrapped into the standard FP representation. The dedicated hardware design extracts the 6-bit format automatically and performs the computation.

3) SoC Design and Compatibility

The proposed design is an alternative for low-power FP inference. The system runs as a cooperative hardware/software mechanism. This architecture delegates compute-bound tensor operations to a hardware accelerator.

The hybrid 32-bit FP and 6-bit FP quantization enables high quality of results and backward ML compatibility. Backwards ML compatibility gives portability from training to inference. This enables to run inference of HF6 quantized models on standard FP hardware and vice versa. Running inference of models without QAT allows rapid deployment; however, this will incur in accuracy degradation, see Fig. 14(c).

4) Future Work

To reduce energy consumption, activation maps can be represented by Bfloat16. This would reduce hardware resource utilization, memory footprint, and data transfer. To increase performance, this implementation would require matching computational throughput with memory bandwidth using systolic arrays to replace the pipeline structure.

VI. CONCLUSIONS

In this paper, we present the Hybrid-Float6 quantization for floating-point CNN hardware acceleration. Feature maps and weights are represented by 32-bit and 6-bit floating-point, respectively. The 6-bit floating-point format is composed of 1-bit sign, 4-bit exponent, and 1-bit mantissa. The 1-bit mantissa enables low-power multiply-accumulate implementations by reducing the mantissa multiplication to a multiplexer-adder operation. We exploit the intrinsic error tolerance of ANN to further reduce the hardware design with approximation. This approach improves latency, hardware area, and energy consumption. To preserve accuracy, we

introduce a quantization aware training method that, in some cases, improves accuracy. We present a lightweight tensor processor implementing a pipelined vector dot-product. For ML compatibility/portability, the 6-bit FP is wrapped in the standard floating-point format, which is automatically extracted by the proposed hardware. The hardware/software architecture is compatible with TensorFlow Lite. We evaluate the applicability of our approach with a CNN-regression model for anomaly localization in a structural health monitoring application. The embedded hardware/software framework is demonstrated on XC7Z007S as the smallest Zynq-7000 SoC. The proposed hardware achieves a peak power efficiency and acceleration of 5.7 GFLOPS/s/W and 48.3×, respectively.

REFERENCES

- [1] M. Lom, O. Pribyl, and M. Svitek, "Industry 4.0 as a part of smart cities," in *2016 Smart Cities Symposium Prague (SCSP)*. IEEE, 2016, pp. 1–6.
- [2] G. Li, C. Deng, J. Wu, X. Xu, X. Shao, and Y. Wang, "Sensor data-driven bearing fault diagnosis based on deep convolutional neural networks and s-transform," *Sensors*, vol. 19, no. 12, p. 2750, 2019.
- [3] F. Dong, X. Yu, E. Ding, S. Wu, C. Fan, and Y. Huang, "Rolling bearing fault diagnosis using modified neighborhood preserving embedding and maximal overlap discrete wavelet packet transform with sensitive features selection," *Shock and Vibration*, vol. 2018, 2018.
- [4] T. Nagayama and B. F. Spencer Jr, "Structural health monitoring using smart sensors," Newmark Structural Engineering Laboratory, University of Illinois at Urbana . . . , Tech. Rep., 2007.
- [5] J. Wang, Y. Chen, S. Hao, X. Peng, and L. Hu, "Deep learning for sensor-based activity recognition: A survey," *Pattern Recognition Letters*, vol. 119, pp. 3–11, 2019.
- [6] Y. C. Kim, H.-G. Yu, J.-H. Lee, D.-J. Park, and H.-W. Nam, "Hazardous gas detection for fir-based hyperspectral imaging system using dnn and cnn," in *Electro-Optical and Infrared Systems: Technology and Applications XIV*, vol. 10433. International Society for Optics and Photonics, 2017, p. 1043317.
- [7] T. Ince, S. Kiranyaz, L. Eren, M. Askar, and M. Gabbouj, "Real-time motor fault detection by 1-d convolutional neural networks," *IEEE Transactions on Industrial Electronics*, vol. 63, no. 11, pp. 7067–7075, 2016.
- [8] O. Janssens, V. Slavkovikj, B. Vervisch, K. Stockman, M. Loccupier, S. Verstockt, R. Van de Walle, and S. Van Hoecke, "Convolutional neural network based fault detection for rotating machinery," *Journal of Sound and Vibration*, vol. 377, pp. 331–345, 2016.
- [9] O. Abdeljaber, O. Avcı, S. Kiranyaz, M. Gabbouj, and D. J. Inman, "Real-time vibration-based structural damage detection using one-dimensional convolutional neural networks," *Journal of Sound and Vibration*, vol. 388, pp. 154–170, 2017.
- [10] X. Guo, L. Chen, and C. Shen, "Hierarchical adaptive deep convolution neural network and its application to bearing fault diagnosis," *Measurement*, vol. 93, pp. 490–502, 2016.
- [11] Z. Du, K. Palem, A. Lingamneni, O. Temam, Y. Chen, and C. Wu, "Leveraging the error resilience of machine-learning applications for designing highly energy efficient accelerators," in *2014 19th Asia and South Pacific design automation conference (ASP-DAC)*. IEEE, 2014, pp. 201–206.
- [12] E. Nurvitadhi, G. Venkatesh, J. Sim, D. Marr, R. Huang, J. Ong Gee Hock, Y. T. Liew, K. Srivatsan, D. Moss, S. Subhaschandra et al., "Can fpgas beat gpus in accelerating next-generation deep neural networks?" in *Proceedings of the 2017 ACM/SIGDA International Symposium on Field-Programmable Gate Arrays*, 2017, pp. 5–14.
- [13] C. Wu, M. Wang, X. Chu, K. Wang, and L. He, "Low-precision floating-point arithmetic for high-performance fpga-based cnn acceleration," *ACM Transactions on Reconfigurable Technology and Systems (TRETS)*, vol. 15, no. 1, pp. 1–21, 2021.
- [14] S. Han, H. Mao, and W. J. Dally, "Deep compression: Compressing deep neural networks with pruning, trained quantization and Huffman coding," *arXiv preprint arXiv:1510.00149*, 2015.
- [15] S. Han, J. Pool, J. Tran, and W. Dally, "Learning both weights and connections for efficient neural network," *Advances in neural information processing systems*, vol. 28, 2015.

TABLE 4. Comparison of hardware implementation with related work.

| Platform | Chunsheng Mei et al. [16] | Chen Wu et al. [13] | BFP [17] | Paolo Meloni et al. [24] | This work |
|-----------------------------------|---------------------------|---------------------|-------------------|--------------------------|-------------------|
| Device | XC7VX690T | XC7K325T | XC7VX690T | XC7Z007S | XC7Z007S |
| Year | 2017 | 2019 | 2019 | 2019 | 2022 |
| Dev. kit cost | \$7,494 | \$1,299 | \$7,494 | \$89 | \$89 |
| Format (activation/weight) | FP 16-bit | FP 8-bit / 8-bit | FP 16-bit / 8-bit | INT 16-bit | FP 32-bit / 6-bit |
| Frequency (MHz) | 200 | 200 | 200 | 80 | 200 |
| Peak power efficiency (GFLOP/s/W) | 18.72 | 115.40 | 82.88 | 2.98 | 5.74 |
| Peak throughput (GFLOP/s) | 202.42 | 1086.8 | 760.83 | 10.62 | 0.482 |
| Wall plug power (W) | 10.81 | 9.42 | 9.18 | 2.5 | 2.3 |
| BRAM 36Kb utilization | 196.5 | 234.5 | 913 | 44 | 15 |
| DSP utilization | 1728 | 768 | 1027 | 54 | 20 |

- [16] C. Mei, Z. Liu, Y. Niu, X. Ji, W. Zhou, and D. Wang, "A 200mhz 202.4 gflops@ 10.8 w vgg16 accelerator in xilinx vx690t," in *2017 IEEE Global Conference on Signal and Information Processing (GlobalSIP)*. IEEE, 2017, pp. 784–788.
- [17] X. Lian, Z. Liu, Z. Song, J. Dai, W. Zhou, and X. Ji, "High-performance fpga-based cnn accelerator with block-floating-point arithmetic," *IEEE Transactions on Very Large Scale Integration (VLSI) Systems*, vol. 27, no. 8, pp. 1874–1885, 2019.
- [18] M. Courbariaux, Y. Bengio, and J.-P. David, "Binaryconnect: Training deep neural networks with binary weights during propagations," *Advances in neural information processing systems*, vol. 28, 2015.
- [19] Z. Lin, M. Courbariaux, R. Memisevic, and Y. Bengio, "Neural networks with few multiplications," *arXiv preprint arXiv:1510.03009*, 2015.
- [20] P. Colangelo, N. Nasiri, E. Nurvitadhi, A. Mishra, M. Margala, and K. Nealis, "Exploration of low numeric precision deep learning inference using intel® fpgas," in *2018 IEEE 26th annual international symposium on field-programmable custom computing machines (FCCM)*. IEEE, 2018, pp. 73–80.
- [21] J. Faraone, M. Kumm, M. Hardieck, P. Zipf, X. Liu, D. Boland, and P. H. Leong, "Addnet: Deep neural networks using fpga-optimized multipliers," *IEEE Transactions on Very Large Scale Integration (VLSI) Systems*, vol. 28, no. 1, pp. 115–128, 2019.
- [22] L. Lai, N. Suda, and V. Chandra, "Deep convolutional neural network inference with floating-point weights and fixed-point activations," *arXiv preprint arXiv:1703.03073*, 2017.
- [23] S. O. Settle, M. Bollavaram, P. D'Alberto, E. Delaye, O. Fernandez, N. Fraser, A. Ng, A. Sirasao, and M. Wu, "Quantizing convolutional neural networks for low-power high-throughput inference engines," *arXiv preprint arXiv:1805.07941*, 2018.
- [24] P. Meloni, A. Garufi, G. Deriu, M. Carreras, and D. Loi, "Cnn hardware acceleration on a low-power and low-cost apsoc," in *2019 Conference on Design and Architectures for Signal and Image Processing (DASIP)*. IEEE, 2019, pp. 7–12.
- [25] C. Gao, A. Rios-Navarro, X. Chen, S.-C. Liu, and T. Delbruck, "Edgedrnn: Recurrent neural network accelerator for edge inference," *IEEE Journal on Emerging and Selected Topics in Circuits and Systems*, vol. 10, no. 4, pp. 419–432, 2020.
- [26] J. Gu, Z. Wang, J. Kuen, L. Ma, A. Shahroudy, B. Shuai, T. Liu, X. Wang, G. Wang, J. Cai et al., "Recent advances in convolutional neural networks," *Pattern Recognition*, vol. 77, pp. 354–377, 2018.
- [27] I. Goodfellow, Y. Bengio, and A. Courville, *Deep learning*. MIT press, 2016.
- [28] D. Zuras, M. Cowlishaw, A. Aiken, M. Applegate, D. Bailey, S. Bass, D. Bhandarkar, M. Bhat, D. Bindel, S. Boldo et al., "Ieee standard for floating-point arithmetic," *IEEE Std*, vol. 754, no. 2008, pp. 1–70, 2008.
- [29] Y. Nevarez, D. Rotermond, K. R. Pawelzik, and A. Garcia-Ortiz, "Accelerating spike-by-spike neural networks on fpga with hybrid custom floating-point and logarithmic dot-product approximation," *IEEE Access*, 2021.
- [30] S. Sikdar, S. Banerjee, and G. Ashish, "Ultrasonic guided wave propagation and disbond identification in a honeycomb composite sandwich structure using bonded piezoelectric wafer transducers," *Journal of Intelligent Material Systems and Structures*, vol. 27, 10 2015.
- [31] U. Kiencke, M. Schwarz, and T. Weickert, *Signalverarbeitung: Zeit-Frequenz-Analysen und Schätzverfahren*. Oldenbourg, 2008.
- [32] R. B. Blackman and J. W. Tukey, "The measurement of power spectra from the point of view of communications engineering — part i," *Bell System Technical Journal*, vol. 37, no. 1, pp. 185–282, 1958.
- [33] D. P. Kingma and J. Ba, "Adam: A method for stochastic optimization," *arXiv preprint arXiv:1412.6980*, 2014.
- [34] U. Xilinx, "Zynq-7000 all programmable soc: Technical reference manual," 2015.
- [35] J. Hrica, "Floating-point design with vivado hls," *Xilinx Application Note*, 2012.
- [36] J. T. Springenberg, A. Dosovitskiy, T. Brox, and M. Riedmiller, "Striving for simplicity: The all convolutional net," *arXiv preprint arXiv:1412.6806*, 2014.

...